Optically Actuated Soft Microrobot Family for Single-Cell Manipulation

Gergely T. Iványi, Botond Nemes, Ilona Gróf, Tamás Fekete, Jana Kubacková, Zoltán Tomori, Gregor Bánó, Gaszton Vizsnyiczai, and Lóránd Kelemen*

Precisely controlled manipulation of nonadherent single cells is often a pre-requisite for their detailed investigation. Optical trapping provides a versatile means for positioning cells with submicrometer precision or measuring forces with femto-Newton resolution. A variant of the technique, called indirect optical trapping, enables single-cell manipulation with no photodamage and superior spatial control and stability by relying on optically trapped microtools biochemically bound to the cell. High-resolution 3D lithography enables to prepare such cell manipulators with any predefined shape, greatly extending the number of achievable manipulation tasks. Here, it is presented for the first time a novel family of cell manipulators that are deformable by optical tweezers and rely on their elasticity to hold cells. This provides a more straightforward approach to indirect optical trapping by avoiding biochemical functionalization for cell attachment, and consequently by enabling the manipulated cells to be released at any time. Using the photoresist Ormocomp, the deformations achievable with optical forces in the tens of pN range and present three modes of single-cell manipulation as examples to showcase the possible applications such soft microrobotic tools can offer are characterized. The applications describe here include cell collection, 3D cell imaging, and spatially and temporally controlled cell–cell interaction.

1. Introduction

Single-cell investigation methods, such as single-cell genetics,[1] proteomics,[2] or morphological classification[3] have risen to the forefront of biological research in the last decade. These methods require physical handling of individual cells on macroscopic scales (for example, using fluorescence-activated cell sorting (FACS)) or with microfluidic systems.[4] Micropipettes[5] and microtraps[6] are tools for holding cells in specific positions, whereas single cells transportation and rotation can be carried out in a controlled manner among others, with active movable microtools, such as substrate-attached[7] and untethered microgrippers,[8] with electrophoretic systems using high-frequency electric fields[9] or with optothermal traps operating with localized laser heating.[10] Optical tweezers (OT) have also been shown to be very effective for direct[11] and indirect manipulation[12] for arranging, observing, and diagnosing single cells. Indirect optical manipulation prevents the cells from photodamage, and because the trapped intermediate object has a higher refractive index, it allows for more precise manipulation. Optically driven cell manipulating microtools have long been reported in the form of simple spheres[13] or more complex, tailor-made structures.[12b,c,14] These tools are characterized as noninvasive and nontethered, unlike micropipettes, or microgrippers, therefore no external physical wiring is necessary for their

G. T. Iványi, B. Nemes, I. Gróf, T. Fekete, G. Vizsnyiczai, L. Kelemen
HUN-REN Biological Research Centre
Szeged Institute of Biophysics
Temesvári krt. 62, Szeged 6726, Hungary
E-mail: kelemen.lorand@brc.hu

G. T. Iványi
Doctoral School of Multidisciplinary Medical Sciences
University of Szeged
Szeged 6720, Hungary

J. Kubacková, Z. Tomori
Department of Biophysics
Institute of Experimental Physics SAS
Watsonova 47, Košice 04001, Slovakia

G. Bánó
Department of Biophysics
Faculty of Science
P. J. Šafárik University in Košice
Jesenná 5, Košice 04154, Slovakia

G. Vizsnyiczai
Department of Biotechnology
University of Szeged
Szeged 6720, Hungary

**ADVANCED
SCIENCE NEWS**

www.advancedsciencenews.com

**ADVANCED
MATERIALS**

www.advmat.de

operation; it allows their use in any segment of a microfluidic channel that can be reached by the focusing objective. Although micropipettes[15] can apply many orders of magnitude larger forces on the cells than optical traps, they have enormous size and have to be physically introduced from outside of the sample volume. Shape-changing gripping microtools were developed in substrate-tethered and nontethered versions to collect or move cells around but they operate either through external wiring or tubing[7] or by changing the pH or temperature of the whole environment[8a,b] limiting their applicability.

Indirect optical manipulation offers precise actuation of the trapped cells with fluctuation around 100 nm due to the achievable optical forces in the range from tens to hundreds of pikonewtons. When complex microstructures are used for cell manipulation,[12b,c,16] they can approximately be as small as the cells (10–30 μm). Probably the most difficult controlled actuation task is when the cell is rotated to an arbitrary orientation and is held there as steadily as possible during, while the experiment is carried out. Dielectrophoretic actuation have been reported to rotate the cells at high speed for 3D imaging, but it can be done only at given locations in the sample space determined by the electrode arrangement, and it lacks the capability of holding the cell steadily in a desired orientation.[9] Recently, opto-thermal cell manipulation schemes were published taking advantage of localized heating-generated force fields.[10] The method requires much lower optical power to trap the sensitive cells than optical tweezers, but in return, the trapping forces are also an order of magnitude lower. One can move, collect or sort particles even of molecular size with the method, but these manipulations are mostly restricted to the 2D plane where the thermal effect is induced with limited possibilities to move to the third dimension. The rotation this method offers is also continuous, lacking the capability for steadily holding a cell at any fixed position. In contrast, with indirect optical manipulation using a properly designed intermediate tool, cells can be turned to any desired orientation and held there as long as necessary with very low fluctuation.[12c] The major drawback of this method is that the cells need to be attached to the microtools usually with biochemical means and they cannot be released afterward.

The current technological status of multiphoton polymerization[17] allows for developing optically actuated microtools in the direction of mobile microstructures, which are deformable with optical trap forces. Deformable structures, often referred to as soft robots, have been reported in many sizes ranging from several millimeters down to tens of micrometers,[8c,18] and are usually built up as multimaterial systems.[8a,19] When such structures are made of only one elastic material, the most straightforward mode of operation is based on recovering their shape after deformation, similar to ordinary lab tweezers.[8c] In single-cell applications, such microtools can be associated with cells by locking on to them via elastic forces generated during structure deformation rather than chemical or biochemical attachment. Elastic deformations also make such associations reversible: the cells could easily be released after performing the required manipulation task. The control over the microtools dimensions and mechanical properties, namely their Young's modulus is critical for their operation: both must be kept low in order to deform the structures with forces typical

of optical manipulations. The smallest achievable feature size with multiphoton polymerization is around 100 nm, and the bulk Young's modulus of most common photopolymers is in the 1–5 GPa range (SU8: 4 GPa, IP-L: 3.9 GPa, IP-S: 5.1 GPa).[20] However, it has been observed that the elastic moduli of polymer wires with submicrometer cross-section are reduced in a material-dependent manner when compared to the bulk value. For photoresist SCR 500 the shear modulus decreased from 150 MPa to the range of 0.39–0.77 MPa for nanowires with 160–240 nm average thickness.[21] The reduction was attributed to both a lower degree of crosslinking and a relatively larger surface area with dangling polymer chains.[22] The decrease is less dramatic for one of the most successful commercial resins, IP-DIP: for the as-polymerized 240–440 nm wide nanowires, the Young's modulus is 0.8–2.4 GPa compared to 4.5 GPa for the factory bulk value.[23] Our previous experiments with OT-assisted deformation revealed that 200 nm wide nanowires made of the photopolymer Ormocomp have a Young's modulus as low as 3.5 MPa, that is ≈300 times lower than the 1 GPa bulk value.[24] Also, nanowires of this material were recently measured to have a Young's modulus as low as 50 MPa.[25] The high elasticity of Ormocomp nanowires was previously utilized to prepare microfluidic flow velocity measuring device[26] and to study single cardiac cell contraction.[27] Its biocompatibility[27,28] makes it a suitable material for preparing soft robots for live cell applications.

In this paper, we show that with the careful design of geometry and fabrication parameters, two-photon polymerization (TPP) can be used to make self-supported, mobile microtools out of the elastic photopolymer Ormocomp that can be deformed with OT. Deformability is achieved by incorporating either a bendable nanorod or a torsion nanostring as the key elastic element into the microtool design. These nanorod and nanostring components are the simplest elastic structures possible, being much more compact and occupying much less space than those introduced earlier in the form of a spiral spring[29] or a helical cross springs.[30] To demonstrate the diversity of potential applications, we present a family of such elastic microtools developed for specific single-cell manipulation tasks. The family includes three members: the first is a cell transporter designed to enclose and move single cells in a microfluidic chamber with no force applied to the cell for its holding. The second microtool is a cell tweezer that is able to hold and spatially manipulate cells with high stability and precision, the capability of which is demonstrated by applying it in multiview microscopy imaging. Finally, the third presented microtool allows for inducing cell-to-cell interactions with precise spatial and temporal control. We show the potential of these microtools by performing proof-of-concept manipulation experiments performed on nonadherent mammalian cells.

2. Results

The deformability of the presented microtools is made possible by the insertion of either bending rods or a torsional string into the structure (**Figure 1**). The bending moment or torque required for their deformation is determined by their geometry and material characteristics (Equations (1) and (2)). For bending two nanorods that span between two rigid rods by applying force at
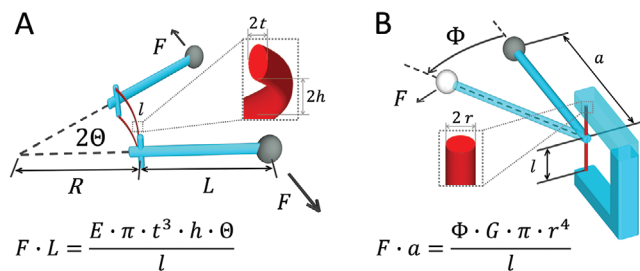
**ADVANCED
SCIENCE NEWS**

www.advancedsciencenews.com

**ADVANCED
MATERIALS**

www.advmat.de

Figure 1. Geometrical model of the deformation of microstructures with A) two nanorods and B) a nanostring as the elastic element (colored red).

their ends as shown in Figure 1A, the bending moment M for small distortions is

$$M \equiv F \cdot L = \frac{E \cdot \pi \cdot t^3 \cdot h \cdot \Theta}{l} \tag{1}$$

where F is the force applied at the two ends, L is the distance between the bending rods and the trapping spheres, E is the Young's modulus, t is half the thickness of the bar, h is half of its height, l is its length, and Θ is the half angle of the two rigid rods;[31] here, for a rod of ellipsoid cross section $t^3 \cdot h \cdot \pi/4 = I$ is called the second moment of inertia, and the bending radius R is expressed as $l/(2\Theta)$.

In the case of a two-end-fixed torsional string (Figure 1B), the torque necessary to twist it at the middle by angle Φ is

$$T \equiv F \cdot a = \frac{\Phi \cdot G \cdot \pi \cdot r^4}{l} \tag{2}$$

where F is the tangential force, a is the arm length, r is the radius of the string, l is the half of its length, and G is the torsional modulus ($G = E/(2 \cdot (1+\nu))$, where ν is the Poisson's ratio, which for most plastics is $0.35 < \nu < 0.45$).[32,33]

2.1. Optical Deformation of the Nanowires

In both cases of elastic elements, their elasticity and the moment or torque exerted by the optical trap's force determine the achievable deformation. Since the available trapping force is limited, the exertable torque can only be increased by the length of the lever arm, which, in turn, will be limited by a practical constraint of avoiding excessively large structures. On the other hand, increasing deformation by making the elastic elements "softer" is undesirable, as it would risk the collapse of the structures during their development and washing. Thus, it is logical to optimize the geometrical parameters of the elastic elements in Equations (1) and (2) to match with the available torque. In order to keep our design's size practical, we use a fixed length l for the flexible element and choose to optimize its thickness parameters (t, h, or r) by tuning the fabrication laser power.

We design all structures with the same trapping sphere-handles with a diameter of $4.5 \pm 0.2 \, \mu m$, that when trapped with the maximum power of our laser tweezer (225 mW per trap at the objective's entrance pupil), it produces a trap stiffness of $30 \pm 1 \, pN \, \mu m^{-1}$. The lever arm lengths were chosen to be between 30 and 50 µm in the various microtools.

2.1.1. Bending Rod

We test the applicability of the bending rods with an "opening" test structure that has a lever arm length of 35 µm and a bending rod prepared with 20 µm s^{-1} scan speed and 4.5–6 mW laser power (**Figure** 2A). COMSOL simulation showed that stress builds only in the elastic part of the structure during deformation (Figure 2B). It also predicted the amount of deformation: as an example, the structure with bending rod dimensions of 400 nm thickness and 1.15 µm height (achievable with fabrication parameters 6 mW power and 20 µm s^{-1} scan speed, Figure S2, Supporting Information) can be bent by 10° with 50 pN force. This value fits well with the measured ones, as shown next. The experiments showed that the force to open these structures increased linearly with the opening angle at all laser powers for small angles (up to ≈15° for 5 mW, ≈8° for 5.5 mW, and ≈4° for 6 mW, Figure 2B). Not surprisingly, the force required to open the structures by the same amount drastically increases with the polymerization laser power: for instance, for 10° opening 2.4, 14.5, 22, and 34 pN is needed in the 4.5, 5, 5.5, and 6 mW cases, respectively; 30° opening can be realized only with the rods made with 4.5 and 5 mW. This is the combined consequence of the increase of rod thickness and height with the laser power, from 0.3 to 0.4 µm and from 0.5 to 1.15 µm, respectively (Figure S1, Supporting Information), and of the increase of the Young's modulus, as explained in the next paragraph. Based on these curves, the parameter couple of 5 mW and 20 µm s^{-1} demonstrated a well-balanced performance suitable for practical use across all the presented structures. This combination allowed easy opening to 30° with a force of ≈45 pN, ensuring mechanical stability to prevent damage or collapse during the development and collection process.

According to Equation (1), the dependencies of force versus opening angle, along with the nanostring dimensions (Figure S1, Supporting Information), provide a way to directly obtain the Young's modulus for the bending bars at each polymerization parameter. Rearranging Equation (1) reveals that, the Young's modulus depends on the F/Θ ratio, which was obtained through a linear fit to the low-angle linear regime of the averaged F versus Θ curves (dashed gray line in Figure 2B). The ratio, as provided by the slope of the fit, increased from 17.6 pN/rad (4.5 mW) to 276.8 pN/rad (6 mW). From these values, the Young's modulus was determined to be between 2.6 and 7.2 MPa, as shown in Figure 2C. It corresponds nicely with the 3.5 MPa value, we determined earlier with a completely different method for nanorods prepared with 6 mW laser power and 20 µm s^{-1} scan speed.[24] The origin of the Young's modulus dependence on the polymerization parameters is beyond the scope of this paper.

2.1.2. Torsion String

The torsion string test experiments were conducted using a surface-mounted test structures bearing a 30 µm long lever arm and a 13 µm long torsion string fabricated with 20 µm s^{-1} scan speed and 4.5–5.5 mW laser power (Figure 2D,E). Here, the simulations also show that the majority of the stress builds up in the nanorod while the rest of the structure is practically unaffected (Figure 2E). The force required for the same amount of distortion increased with the polymerization laser power once again:
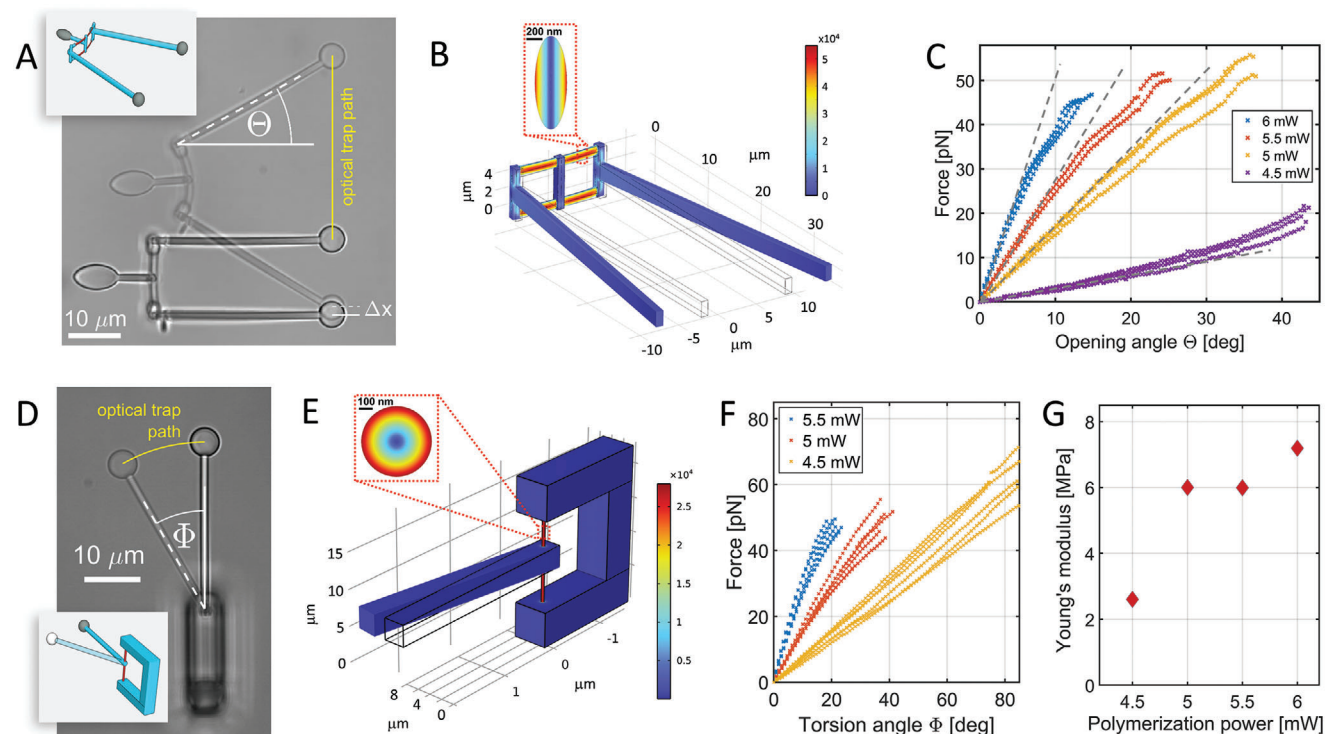
2401115 (3 of 12)

**ADVANCED
SCIENCE NEWS**

www.advancedsciencenews.com

**ADVANCED
MATERIALS**

www.advmat.de

Figure 2. Optical forces necessary to deform the bending rods and torsion strings. A) Overlaid optical microscopic images of a rod bending test structure in its relaxed and open states; the inset shows the scheme of the open state. The yellow line shows the path of the upper trap that was followed by the upper trapping sphere. The Δx displacement of the stationary sphere, used for force calculation, is also shown. B) The von Mises stress distribution calculated in COMSOL Multiphysics for the bending test structure when a pair of 50 pN opening forces are applied to the ends of the two arms. The 3D model dimensions fit to the 6 mW power and 20 μm s^{-1} scan speed experimental structure. The stress in the cross section of the elastic rod is shown in the inset. The color bar values are expressed in N m^{-2} units. C) The measured optical force acting on each trapping sphere as the function of the measured opening angle. Results are shown for bending rods polymerized with different laser powers (4.5–6 mW as shown in the legend). The gray dashed lines show the linear fit to the averaged curves. D) Overlaid optical microscopic images of structure II in its relaxed and distorted states. The inset shows the overlaid schemes of these states. E) The von Mises stress distribution calculated in COMSOL Multiphysics for the torsion test structure deformed by a force of 20 pN applied to the end of the deflecting arm. The 3D model dimensions fit to the 5.5 mW laser power and 20 μm s^{-1} scan speed (440 nm) experimental structure. The inset shows the stress distribution inside the flexible part. The color bar values are expressed in N m^{-2} units. F) The optical force acting on the trapping sphere of the torsion test structure as the function of the measured torsion angle. Results are shown for torsion strings polymerized with different laser powers (4.5–5.5 mW as shown in the legend). G) The Young's moduli of the nanorods calculated by Equation (1) as the function of laser power (scan speeds 20 μm s^{-1} for all). D) Overlaid optical microscopic images of structure II in its relaxed and distorted states. The inset shows the overlaid schemes of these states.

strings made with 5.5 mW can be twisted up to 15°–20°, while those made with 4.5 mW to more than 90°. The initial linear parts of the force versus angle plots have slopes of 3.17 pN deg^{-1} for 5.5 mW, 1.57 pN deg^{-1} for 5 mW and only 0.71 pN deg^{-1} for 4.5 mW. When normalized with the rod length, a more general value is resulted describing the torsion string itself: it is 95.1, 47.1, and 21.3 pN deg^{-1} μm^{-1} for the strings polymerized with 5.5, 5, and 4.5 mW laser power, respectively. When a structure based on the torsion string mounts a cell to the substrate (see Section 2.4 below), one can easily calculate the force that keeps the cell in place by measuring the twisting angle relative to equilibrium and the lever arm's length between the string and the cell surface.

2.2. Collecting Cells: Cell Transporter

The purpose of the cell transporter structure (structure III, see the Experimental Section) is to selectively collect single, nonad-

herent cells in a microfluidic environment and deposit them to a predefined location without applying significant force on them (**Figure 3A**). The wireframe design of the cages (Figure 3C) was intended to reduce the viscous drag on the structure during transportation. As a result, using the maximum trapping laser power, the structures can be translated at speeds up to 300 μm s^{-1} in the direction parallel to their main axis and 200 μm s^{-1} perpendicular to it. The two halves of the 30 μm diameter cages could be easily opened to larger than the typical cell diameter (12–18 μm), allowing the transporter to enclose and pick up cells without difficulty.

The scheme of the process of cell collection is shown in Figure 3A and snapshots of the actual experiment in Figure 3B (see also Movie S1, Supporting Information). The target cell is selected visually from the ensemble of cells settled on the glass substrate. The cell transporter, trapped at three points, approaches it by moving the microscope stage. Then the OT opens up the transporter structure, forming a gap somewhat larger than the cell size between the two cages. Moving the stage, the cell is maneuvered in between the cages which then are closed ("collect"). After this
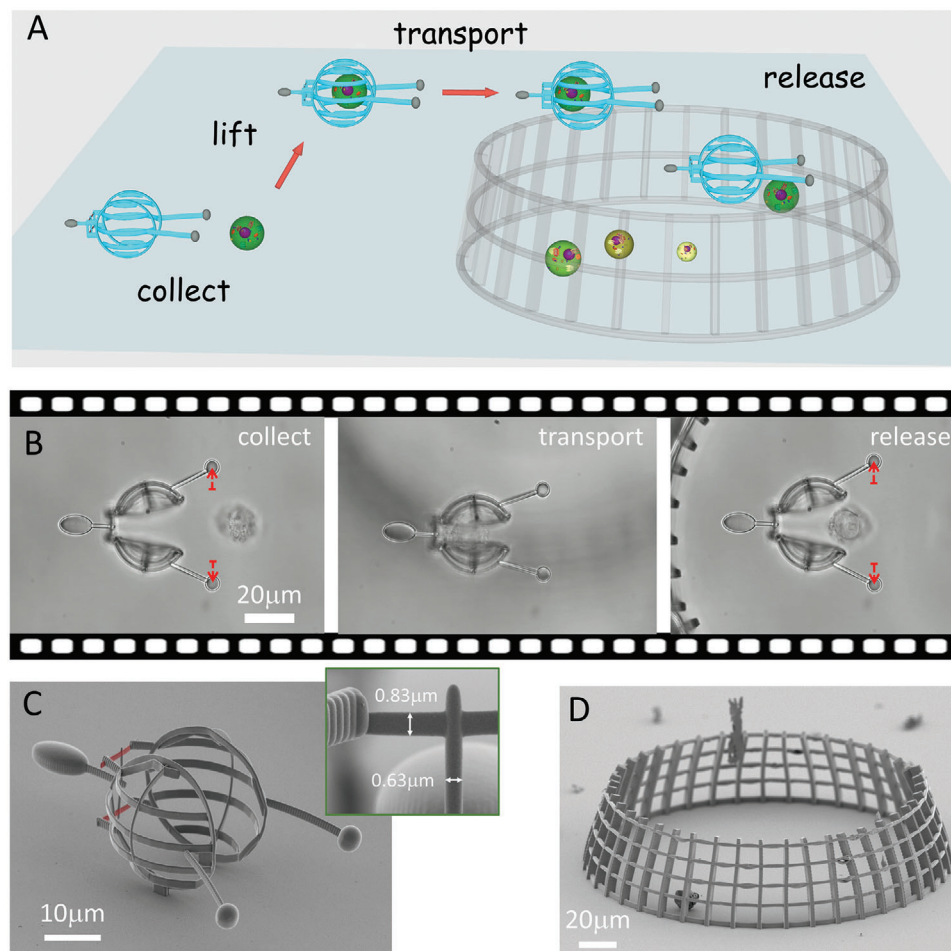
**ADVANCED
SCIENCE NEWS**

www.advancedsciencenews.com

**ADVANCED
MATERIALS**

www.advmat.de

Figure 3. Single-cell collection with optically actuated microstructure. A) The scheme of the cell collection procedure. B) Brightfield microscopic images of the major steps of the collection procedure (Movie S1, Supporting Information). The red arrows indicate the direction of the optical trap's movement for opening up the structure. The defocused image of the cell container's rim is visible during transport. C) The electron micrograph of the cell mover with the elastic rods overlaid with red. The inset shows the height of the bending rod (0.83 μm) and the thickness of the vertical rod (0.63 μm) that connects the two bending rods and supports the trapping ellipsoid. D) Electron micrograph of the cell container.

point, the traps serve only to move the structure and the cages are kept closed around the cell merely by elastic forces. Next, while holding the structure with the OT, the cell transporter is lifted from the substrate by moving the focusing objective ("lift"). The structure is then transported toward the targeted container at a height that is higher than the height of its fence (Figure 3D) by moving the sample stage ("transport"). The noticeable displacement of the cell inside the cage shows that the structure does not squeeze the cell at all, which is the main advantage of cell translation with this structure. After maneuvering the cell transporter over the container's fence, it is lowered slightly below the height of the fence. The cell is released here by opening the cell transporter ("release") with the OT. At this point, the cell slowly rolls out of the cage and falls to the bottom of the container. One cell collection cycle between two consecutive cell collection steps lasts about 3 min.

The compactness of this structure is limited by a minimum distance between the trapping spheres and the cell containing cage. When it is too small, during cell release, the radiation pressure of the strongly focused trapping beam pushes the falling cell

up toward the spheres eventually blocking the beam and causing the OT to release the structure; a minimum of 20 μm cage-to-sphere distance was therefore necessary. For similar reasons the cell transporter structure may not be moved lower than 30 μm above the substrate during cell release as the radiation pressure of the trapping beam would push the already settled cells toward the cell transporter's spheres. Considering maneuvering, it is crucial that the vicinity of the target cell is not crowded with other cells during the collection step, as they may interact with the OT.

2.3. Imaging Cells: Cell Tweezers

For applications where it is crucial to hold a cell with minimal fluctuations (for instance imaging), we introduce the elastic cell tweezers structure (**Figure 4A,B**). We previously demonstrated the benefit of indirectly trapping a single cell with a polymer microtool for precise 3D imaging.[12c] In the procedure introduced here, the tweezer tool's elasticity, rather than a chemical or biochemical attachment, keeps the cell attached to the structure.
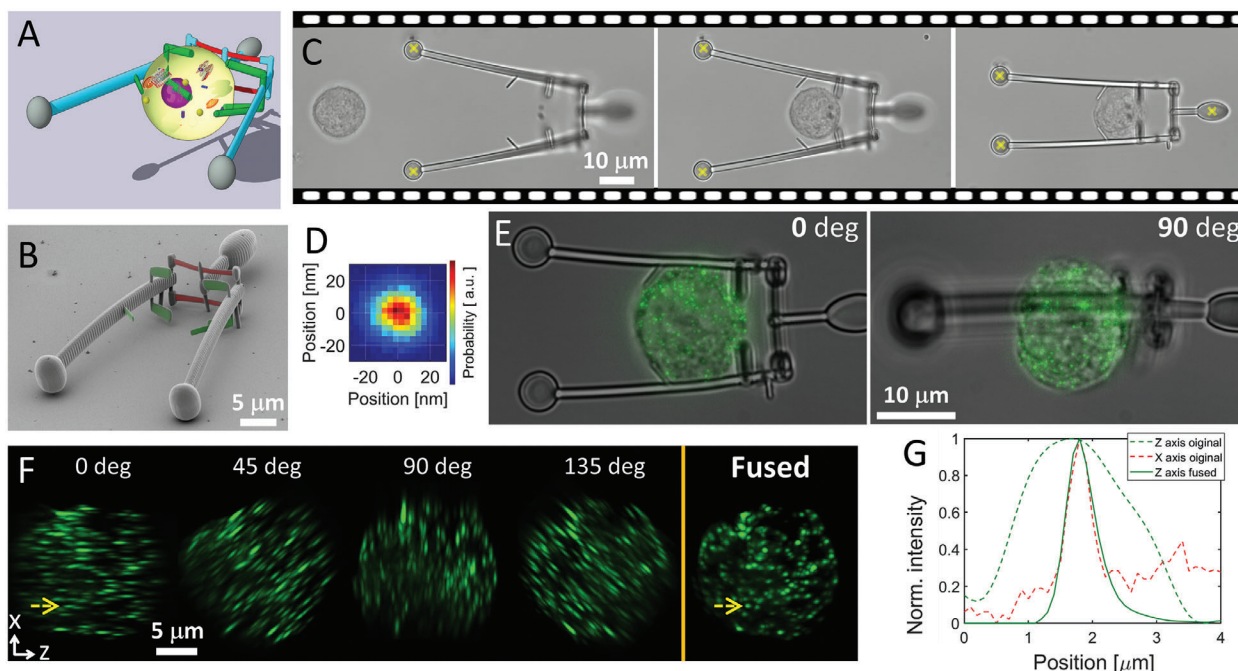
**ADVANCED
SCIENCE NEWS**

www.advancedsciencenews.com

**ADVANCED
MATERIALS**

www.advmat.de

Figure 4. Cell tweezers structure and its application for multiview microscopic imaging. A) Schematic view of the nonadherent cell held with the cell tweezers structure. B) Electron micrograph of the cell tweezer structure; the flexible rods are highlighted with red, the cell holding pins with green. C) Brightfield microscopy snapshots of the cell collection procedure. The yellow stars mark the position of the OTs. D) Fluctuation of a cell measured in a stationary position held with an optically trapped tweezers structure. E) Brightfield-fluorescence composite images of a fluorescent nanobead-labeled cell held with the tweezers structure in two different orientations reached by rotating the microstructure by 90° with the OT. F) Maximum intensity projection images of aligned image stacks recorded on fluorescent bead-decorated cells originating from four different orientations and that of the fused image stack. G) Normalized intensity traces observed along the Z and X axes on the bead marked with a yellow arrow on panel (F). The more than three times reduction of the image width along the Z axis demonstrates the resolution enhancement.

Another natural advantage of the nonpermanent attachment is that the cell can be released after inspection (see Movie S2, Supporting Information). We demonstrate the capabilities of the new cell tweezers microtool with 3D imaging using multiview microscopy. The imaging task naturally demands that the microtool does not distort the image of the cell. Consequently, it was constructed with a minimum number of elements, each as thin as possible. The negligible residual distortion is illustrated in Figure S2 (Supporting Information). Fluorescent nanobeads attached to the cells were used to assess the imaging quality.

Picking up a cell with the tweezers structure (Figure 4C) was similar to the process shown for the cell transporter tool. First, a cell with enough nanobeads on it was selected using fluorescent observation. Then, in brightfield mode, the trapped tweezers structure approached the cell, it was opened up, the cell was maneuvered in between the small pins of the microtool, and finally the OT closed them onto the cell. At this stage the pins touch the cell's surface, and the microtool's elasticity alone can hold them together. We occasionally had to move the trapping spheres closer to one another with the OT to hold the cells more firmly to reduce their fluctuation. For precise imaging, the tweezed cell's spatial stability must be good enough not to cause blur, which we quantified by holding a cell stationary and observing its position (Figure 4D). Approximately 5000 frames were recorded, and a correlation algorithm was used to determine the cell's movement. The widths at the half of the maximum of the cell's position probability were 24.75 and 23.9 nm along the axes X and Y,

respectively, both being small enough to allow for high-resolution imaging even with long exposure times. The force each holding pin exerts on the cell surface can be estimated from the dependence of the optical force on the opening angle of the structures (Figure 2B), the length of the rigid rods and the distance of the cell from the bending rods. Considering the various angles between the two rigid rods when cells of different diameter are entrapped between them (from 3° to 11.5°), we estimated that each pin exerts a force between 4 and 15 pN on the cell; the higher value is expected for the larger cells (for details see Figure S3, Supporting Information).

Multiview microscopic imaging requires independent Z-stack recordings of the cell in multiple orientations that are achieved by rotations around an axis perpendicular to the optical axis. Figure 4E depicts such a case in which the cell is rotated around the X axis by 90° to a new orientation by actuating the optically trapped cell tweezers. In our case, the Z-stack image series were recorded in orientations 45° from one another. The processing of the independent Z-stack image series was carried out as previously described.[12c] Shortly, an iterative 3D deconvolution step with 40 iterations (Richardson–Lucy algorithm) was performed first, followed by a registration process of the image stacks with a direct search algorithm, aligning the different orientations to the first, 0° orientation. The first four images in Figure 4F show the result of the deconvolution and alignment steps; it displays the significant elongation of the bead images as the result of the inherent anisotropic resolution of the fluorescent microscope. The
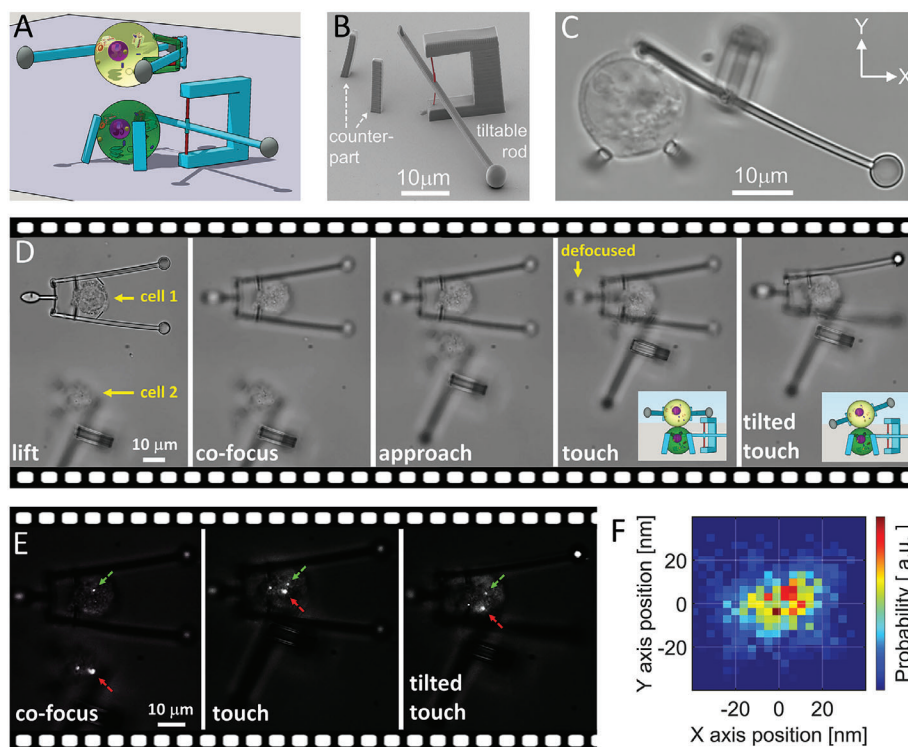
**ADVANCED
SCIENCE NEWS**

www.advancedsciencenews.com

**ADVANCED
MATERIALS**

www.advmat.de

Figure 5. Cell–cell interaction with indirectly trapped cells in the vertical direction. A) Schematic draw of the interaction: the lower cell is substrate-attached, while the upper one is optically maneuvered. B) Electron micrograph of the cell-retaining structure; the flexible string is highlighted with red. C) Brightfield image of a substrate-mounted cell. D) Stages of the cell–cell interaction procedure; for explanation, see main text. For "tilted touch," the structure was tilted by 15°. E) Cell–cell interaction experiment with fluorescently labeled cells observed with a combination of fluorescent imaging and a weak background illumination to visualize the cell manipulating microstructures. The red arrow points to a nanobead selected on the surface-mounted cell, while the green arrow points to one attached to the cell held with the tweezers structure above the mounted one. F) Position distribution of a substrate-mounted cell, similar to that shown in panel (C), due to its residual fluctuation after it being pressed against the two vertical bars.

final fusion process was carried out by the pixelwise multiplication of the aligned image stacks, yielding a single 3D stack of isotropic optical resolution (Figure 4F "Fused"). The resolution enhancement is demonstrated qualitatively by the nonelongated images of the nanobeads and quantitatively in Figure 4G by plotting the intensity traces over a selected bead along the Z axis from the as-recorded stack and from the fused one. The width of the intensity peak is reduced from about 2.1–0.6 μm.

2.4. Cell–Cell-Interaction Using a Pair of Structures

We present two modes for realizing cell-cell interactions, one with axial and one with lateral direction of approach (**Figures 5A**, and **6A**). Both approaches rely on a pair of OT-actuated cell manipulator structures: a surface-mounted cell-retaining microtool, and a mobile microtool. The cell-retaining microtool is used to anchor one cell to the substrate in a fixed position, while the second one to maneuver and push another cell against the first cell either from the side or from above. Because precise spatiotemporal control of these cells is critical, they must be held with minimal fluctuation.

The cell-retaining microtool operates on the torsion force risen in a distorted string (Figure 5B,C). A tiltable rod is attached to this string with one end equipped with a sphere for the OT, while the

other end presses the cell against a substrate-mounted counterpart. To allow for the lateral and axial approaches, two types of counterparts were designed, each leaving the respective surfaces of the cell freely accessible. In the axial approach, the counterpart is simply a pair of slightly tilted columns, while in the lateral approach it is a ring with a plane perpendicular to the substrate glass. Cell capturing (Movie S3, Supporting Information) begins with tilting the rod with the OT against the string's torsion resistance, followed by moving the cell in between the other end of the rod and the counterpart with another trap. This second trap directly illuminates the cell for a few seconds, however such a short exposure is unlikely to cause damage to the cell.[34] When the trap is turned off, the rod's end pushes the cell against the counterpart. This cell-retaining force is controlled by the polymerization parameters of the string as shown in Figure 2E, and Figure 5F depicts cell fluctuation as held by the retaining structure. It was found to be 40 and 30 nm along the X and Y axes, respectively; the smaller fluctuation along the Y axis can be explained by the cell being pressed against the counterpart along this axis.

In the vertical approach the mobile microtool was the cell tweezers structure described in the previous section. Fluorescent bead-decorated cells were used to better track the axial position of the overlapping cells. At the beginning of the process (Figure 5D; and Movie S4, Supporting Information), the upper surface of the substrate-mounted cell and the bottom surface of the optically
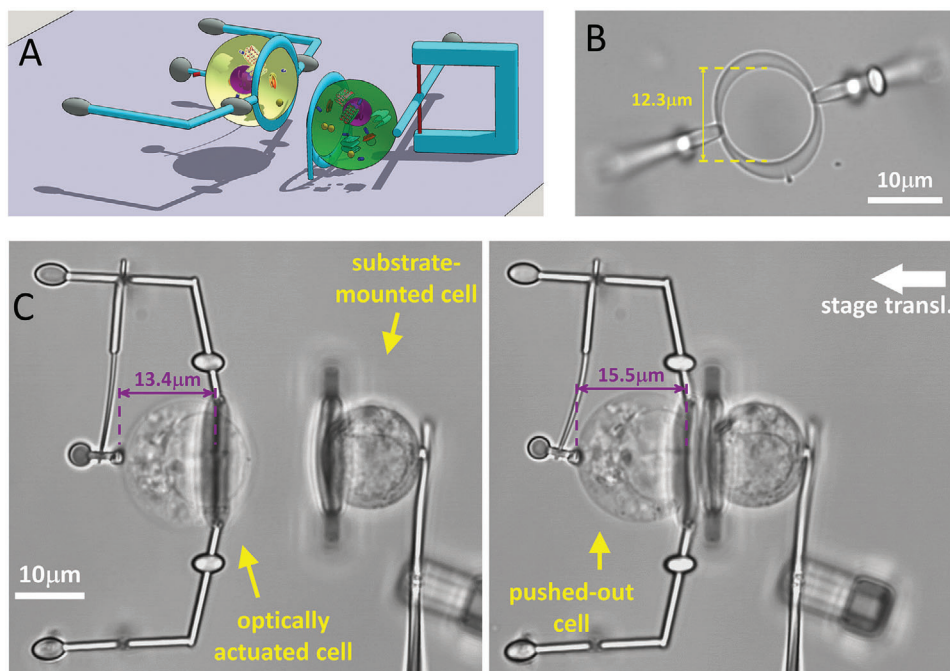
Figure 6. Cell–cell interaction with cells translated in the lateral direction. A) Arrangement of the cells held by the two types of structures. B) Brightfield image of the ring of the cell holding structure VI. C) Brightfield optical microscopic image of the cell–cell interaction with lateral movement. On the left, the two cells are separated; the stage moves the substrate-mounted cell in the direction of the thick white arrow. On the right, the two cells come into contact, and the optically manipulated one is slightly pushed out by the other one. The distance between the accommodation ring and the retaining pin is highlighted in purple.

actuated cell were brought into a common focal plane ("co-focus") by moving the focusing objective ("lift") and the optical traps vertically. Next, the lower cell was transferred underneath the upper one by moving the microscope stage ("approach"). For the interaction, the optically actuated cell was lowered by the focusing objective to touch the lower cell ("touch"). This step pushed the mobile cell slightly upwards as evidenced from the additional defocusing of the trapping ellipsoid in Figure 5D. The two cells can even slide over each other at this position by moving the stage sideways. This kind of interaction is evidenced by the slight lateral displacement of the upper cell. The ability to hold the upper cell in various orientations (Figure 5D,E, "tilted touch") allows to change its contact surface presented to the other cell. The vertical approach allows for the entire interacting membrane regions to be observed in the image plane.

The lateral approach was conceived with the advantage in mind that the cell images do not overlap, so the effects of the interaction can be observed undisturbed in both cells. For this approach, a special structure was designed (Figure 6A,B) that is holding the cell with the elastic force of a bent rod that pushes the cell against a ring. To grab a cell, the elastic rod is pulled away from the ring by the OT, allowing a cell to be maneuvered into the space between the two (see Movie S5, Supporting Information). Finally, the trap is turned off, the elastic rod relaxes, and the cell is captured. Once the cell is mounted, the structure is maneuvered by the OT holding the four trapping ellipsoids.

To start the interaction, the movable cell is held steadily with the OTs, and the substrate-mounted cell is pushed against it by slowly translating the microscope stage (see Figure 6C; and Movie S6, Supporting Information). During this, the circumfer-

ence of the cells are usually brought into a common focus, but their mutual position along the optical axis can also be varied to some extent. It was frequently observed that one of the cells pushes the other slightly out from its accommodation ring; in Figure 6C, ≈2 µm of such movement is seen. In these cases, the elastic element held the cell in place and returned it to its original position after separation. Structure VI is designed in such a way that mechanical forces exerted during the interaction can be measured with it, however, it was beyond the scope of the present paper. A possible scenario is that the two cells bind to each other after making a controlled contact. The structure's ring and the four trapping ellipsoids are arranged, so that if the two attached cells have to be separated, a large pulling force can be exerted without allowing the mobile cell to slip out of the structure due to the ring's diameter being significantly smaller than that of the cell. In this case, while the substrate-mounted cell is pulled away by moving the microscope stage, the position of the optically held structure can be used to measure the force between them at the moment of their detachment.[35]

3. Conclusion

Deformable microtools prepared with multiphoton polymerization and actuated with optical tweezers were introduced in proof-of-concept single-cell manipulation experiments. The key components of the microtools are elastic nanorods that can be bent or twisted, acting as hinges for the rigid parts of the structures. The prepared structures can be deformed with optical forces of no more than 60 pN when the fabrication parameters are carefully balanced, resulting in elastic rod cross sections of a few hundred
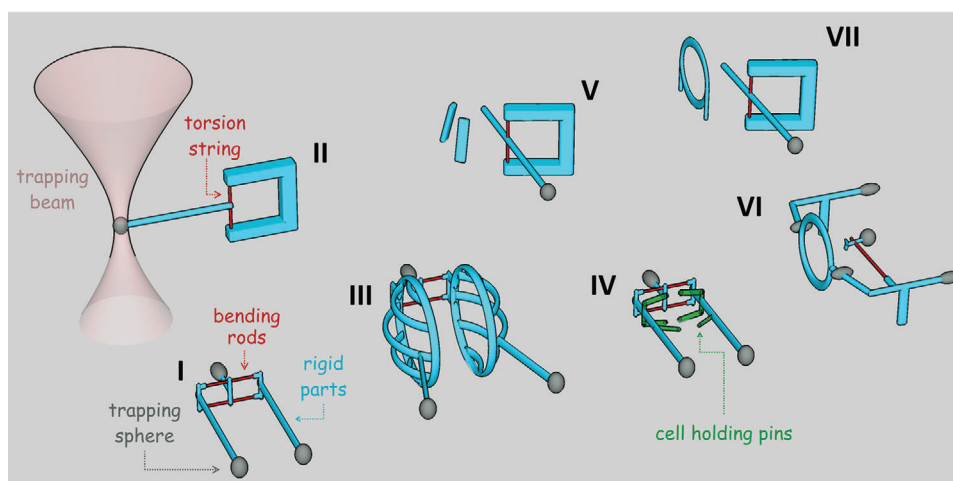
Figure 7. Schematic representations of the elastic, deformable microstructures used in the experiments. See the main text for a more detailed description. Structures I and II were used for the bending and torsion tests, while structures III-VII for cell manipulation. The focused beam of the optical tweezers is illustrated with structure II as it is trapping its trapping sphere.

nanometers. At the same time, these structures proved to be reasonably stable in terms of shape integrity under the load of the moving liquid during the fabrication procedure. A fundamental feature of the microtools is that the microtool-cell association is not permanent, meaning that when the required task is finished, the structures can eventually release the cells. First, the microtools were used to select, capture, and collect cells to a predefined location inside a microfluidic system, using 3D translation, without exerting considerable force on the cells. Second, fluorescence multiview imaging with firmly captured cells actuated with 6° of freedom and with better than 50 nm precision was demonstrated. Finally, cell–cell interaction was demonstrated in two directions of approach, vertical and lateral, with mounting one of the cells to the bottom surface of the microfluidic channel and maneuvering the other one to it for touching with precise temporal and spatial control. The completed tasks demonstrated that multiphoton polymerization combined with optical manipulation can prepare and actuate tools for complex soft-robotics applications in the field of single-cell research.

4. Experimental Section

Microstructure Polymerization: The elastic cell manipulator structures were fabricated by two-photon polymerization (TPP) using a custom-made setup.[24] The essential elements of the setup are an ultrashort-pulsed fiber laser (λ = 785 nm, pulse length = 100 fs, C-Fiber A, Menlo Systems, Germany) as light source, a high NA objective (40x oil, 1.3 NA, C Plan-Apochromat, Zeiss, Germany) that focuses the beam into the Ormocomp (Microresist GmbH, Germany) photopolymer, a 3-axis piezo stage (P-124 731.8L and P-721.10, Physik Instrumente GmbH, Germany) for nanometric translation of the sample relative to the focus and an acousto-optical modulator to change the power of the polymerizing laser beam (APE 130 101, APE GmbH, Germany). The TPP system was controlled by a Labview program. The Ormocomp microstructures were polymerized onto standard glass cover slides (Menzel Gläser, Germany). A plastic ring of 2 mm height and 10 mm diameter was glued to the center of the cleaned slides with Norland optical adhesives (NOA81, Thorlabs Inc, USA) and a 1 μL droplet of Ormocomp was drop-casted at its center. The plastic ring ensures that the polymerized microstructures remain in liquid throughout the development and sample preparation procedure preventing their

collapse. After the polymerization, the sample was rinsed in Ormocomp's developer solution (Ormodev, Microresist GmbH, Germany) for 10 min twice and then transferred to ethanol for another 2 times 10 min rinse. During the second bath in the developer, the entire sample was illuminated with a microscope mercury lamp (HBO50) to facilitate postpolymerization.

First, test lines were polymerized both in lateral (referred to as rods) and axial direction (strings). The parameter matrix for the rods ranged from 4 to 9 mW laser power and from 1 to 100 μm s^{-1} scan speed; for the strings these ranges were 4–7 mW and 3–100 μm s^{-1}. The 10 μm long rods were polymerized 7 μm above the substrate between supporting blocks, while the 11 μm long strings were polymerized inside a thick vertical frame (see Figure S1D, Supporting Information). The test lines were critical point dried (CPD) for scanning electron microscopy (SEM) imaging. Their cross-section dimensions were determined with the ImageJ software.

Structures for Elasticity Test: All the deformable microstructures (**Figure 7**) consisted of three main regions: i) deformable rods or strings (colored as red), ii) spheres that interact with the optical trap (designed with 4 μm diameter, colored as gray) and iii) rigid, nondeformable elements (colored as blue).

For the optical deformability tests, two different types of structures were designed. The first type tested the bending elastic rods (Figure 7, structure I). These structures consisted of two 35 μm long rigid rods, connected at one end by two 10 μm long parallel bending rods; the two rods were needed for structural stability and in-plane only motion. The scan speed for the polymerization of the bending rods was 20 μm s^{-1}, while the laser power was varied from 4.5 to 6 mW. A trapping sphere was polymerized at the other end of each rigid rod. The rods were bent, therefore the structure was opened simply by moving one of the spheres by translating the corresponding optical trap away from the other (yellow line in Figure 2A). During translation, two parameters were monitored by video microscopy: the increasing angle between the rigid rods (2Θ on Figure 1A) and the position of the stationary sphere. As the translated sphere moves, the elastic stress risen due to the bending nanorods applies a force on both trapping spheres, which is balanced by the trapping force. The two spheres are held by optical forces of the same amplitude but opposite directions (forces *F* on Figure 1A). In the resting state before the opening of the structure, the center of the stationary sphere assumes the position of the nontranslating trapping focus. During opening however, the elastic force pulls this sphere out of the resting position with a measurable Δ*x* displacement. The optical force *F* required for the opening was obtained by multiplying this displacement by the *k* trap stiffness of the sphere (measured separately) using the expression $F = -k \cdot \Delta x$.

The second type tested the torsion of the vertical strings. This structure (Figure 7, structure II) consisted of a rigid frame to the torsion string, the string itself and a horizontal rigid rod attached perpendicularly to the center of the string. The 13 µm long string was prepared with 20 µm s^{-1} scan speed using 4.5, 5, and 5.5 mW laser power. The 3 µm long thick middle section of the string was needed to attach the rigid rod to it. The trapping sphere was prepared at the end of the 30 µm long rod. The string was twisted by moving the sphere with the optical trap along the circumference of a circle with a radius of 30 µm (yellow line in Figure 2D) in 1° steps (0.53 µm steps along the circumference). In the resting position, again, the sphere's center coincides with the trapping focus position. During twisting, as the trapping focus moves through predetermined positions, it carries the sphere with it, which distorts the torsion string via the rigid rod. As a result, the stress risen in the string displaces the trapping sphere's center from the trapping focus position. The force required to distort the string was calculated from this Δx displacement, and from the separately measured k trap stiffness of the sphere.

Cell Manipulator Structures: Three microstructures were prepared for three distinct cell manipulation tasks. The elastic parts (bending rods and torsion strings) in all the structures were polymerized with 5 mW laser power and 20 µm s^{-1} scan speed, the trapping spheres with 8 mW and 32 µm s^{-1} and the rigid parts with 8 mW and varying scan speed.

The first structure, the cell transporter (Figure 7, structure III), consists of two half sphere-shaped cages with a diameter of 30 µm each. The cages are connected by two bending rods and can encapsulate a nonadherent cell of about 12–18 µm without squeezing them. The cages are made up of thin lines to reduce viscous drag. A trapping sphere is attached to each cage with a 20 µm long rigid rod. An extra ellipsoid was added to the structure to hold it steadily when lifted from the surface with three optical traps. A cell container structure of 200 µm diameter was also polymerized where the cell transporter could collect the selected cells. It was large enough to accept the entire cell transporter structure and its 50 µm height and the slightly inward-tilted wall ensured that the cells could not migrate passively over it.

The cell tweezers structure (Figure 7, structure IV) is based on the rod bending test structure but it is completed with cell holding pins. Its purpose is to attach a cell to itself to prevent the cell from moving relative to the structure. As a result, the cell precisely follows every movement made with the tool. There are altogether six 5 µm long pins (three on each rigid rods) to anchor the cell firmly to the trapped microstructure. The structure is opened similarly to test structure I with two traps, and an extra ellipsoid was also added for the 3D manipulation using three traps.

The cell-retaining structure (Figure 7, structure V) is based on the torsion string test structure but has been modified at three points. First, the long rigid rod extends to both sides of the torsion string. At one end, the trapping sphere is attached, while the other end is designed for holding the cells. Second, the string-holding frame structure is rotated to form a 70° angle with the long rigid rod. Finally, two slightly tilted substrate-mounted bars are added. These bars provide support against which the free end of the rigid rod pushes the cell.

The cell holding structure type VI is designed for cell-to-cell interaction via lateral movement. The central ring part of this structure accommodates the cell which is pushed against the ring by a short rod completed with a trapping sphere. The short rod is attached to the end of the elastic part of the structure, a bending rod and can be moved with the optical tweezers to create space for the cell. The elasticity of the bending rod pushes the cell against the ring after the trap is turned off. The ring diameter allows the cell to protrude on the other side presenting a surface for interaction with another cell. The four symmetrically positioned trapping ellipsoids allow for complete optical manipulation, especially for pushing and pulling the cell. Structure VII is the counterpart of structure VI and can mount a cell to the substrate by using a ring to accommodate the cell.

The development of the structures shown in Figure 7 is finished differently than that of the test lines. After the ethanol rinse, the structures were transferred to deionized water via the following water-ethanol mixture series: i) 100% ethanol, ii) 66% ethanol, 34% water, iii) 33% ethanol, 67% water, iv) 100% water; the sample was rinsed in each mixture for 1 min. After this, the deionized water was replaced with 1% w/w BSA in 1X PBS. For the opening and torsion test experiments, no cells were used. The rod bending test structures, the cell transporter, and the cell tweezer structures were released mechanically from the substrate with a glass micropipette. The cells were of the type K562 (LGC Standards, UK, cat no. CCL-243),[12c] fixed with 4% formaldehyde and kept in 1X PBS for short-term storage at 4 °C. Whenever cells were used, they were added in the form of 2 µL suspension to the ≈200 µL BSA solution covering the structures previously released from the substrate. After adding the cells, a cover slide was placed over the sample contained within the plastic ring to eliminate the free liquid surface.

Optical Tweezers Setup: The optical tweezers (OT) setup used for the present experiments was introduced earlier in detail.[12c] A wide-field fluorescence microscope (Nikon Eclipse Ti) combined with a holographic optical tweezers setup was used for observing and actuating the structures. The trapping laser beam (THFL-1P400-COL50, BKtel Photonics, France) was manipulated by a spatial light modulator (Pluto NIR, Holoeye, Germany) to create and move multiple trapping focal spots in the sample chamber. The beams were focused into the sample by an Olympus microscope objective (UPlanSApo, 60x, water immersion, NA 1.2). The positions of the trapping focal spots were controlled by a home-made software. The microstructures and the cells were observed in bright field (GS3-U3-23S6M CCD camera, Point Grey Research Inc., Canada) and in fluorescent (ORCA Flash 4.0v3 CMOS camera, Hamamatsu, Japan) mode. The fluorescent light source was a metal halide lamp (Lumen 200S, Prior Scientific, Inc., USA). The positions of the trapping spheres were determined with correlation-based image analysis routines written in MATLAB.

The process of recording and analyzing multiview images was described in detail earlier.[12c] Shortly, Z-stack image series of the fluorescent bead-decorated and optical trap-actuated cells were recorded at predefined orientations, resulting in five 3D recordings of the bead images. The image analysis started with the 3D deconvolution of the stacks with a recorded point-spread function of the microscope. Then, the stacks were aligned to each other, using a direct search algorithm. In the final step, the aligned stacks were fused by the pixelwise multiplication of the aligned stacks.

The calculation of the trap stiffness for the microstructures' trapping spheres was based on bright-field microscopy recordings of the fluctuation of trapped, nontethered spheres using 0.5 ms exposure time. The stiffness (k) was calculated from the variance (σ) of the sphere position data using $k = k_B T/\sigma'^2$ where k_B is the Boltzmann constant and T is the absolute temperature.[36]

Numerical Simulations: Numerical simulations were run in COMSOL Multiphysics. The goal was to see the stress distribution within the microstructures under typical experimental load conditions. Furthermore, cells held by the microstructures were modeled to determine the extent of their deformation and the stress induced in them. The numerical model for the microstructures used Young's moduli of 7.2 MPa for the bending rods, 6 MPa for the torsion strings, and 1 GPa for the rigid elements and line dimensions that were obtained by scanning electron microscopy (Figure S1, Supporting Information). The model for cell deformation used a 15 µm diameter spherical cell with a 10 µm diameter nucleus. The Young modulus of K562 cells was previously measured to be 40[37] or 400 Pa.[38] In the present simulations, 100 and 200 Pa Young's moduli for the cell and nucleus, respectively, were chosen. The cell was pushed against a solid ring by a 1 µm diameter bead with a total force of 10 pN. This configuration replicates the experimental conditions of structures VI and VII.

Supporting Information

Supporting Information is available from the Wiley Online Library or from the author.

Acknowledgements

**ADVANCED
SCIENCE NEWS**

www.advancedsciencenews.com

**ADVANCED
MATERIALS**

www.advmat.de

Conflict of Interest

The authors declare no conflict of interest.

Data Availability Statement

The data that support the findings of this study are available from the corresponding author upon reasonable request.

Keywords

[1] V. K. A. Sreenivasan, S. Balachandran, M. Spielmann, *J. Med. Genet.* **2022**, *59*, 827.

[2] M. Labib, S. O. Kelley, *Nat. Rev. Chem.* **2020**, *4*, 143.

[3] Z. Mousavikhamene, D. J. Sykora, M. Mrksich, N. Bagheri, *Stem Cells Int.* **2021**, *11*, 24375.

[4] a) T. Chen, C. Huang, Y. Wang, J. Wu, *Chin. Chem. Lett.* **2022**, *33*, 1180; b) B. Sarno, D. Heineck, M. J. Heller, S. D. Ibsen, *Electrophoresis* **2021**, *42*, 539.

[5] R. Salánki, C. Hős, N. Orgovan, B. Péter, N. Sándor, Z. Bajtay, A. Erdei, R. Horvath, B. Szabó, *PLoS One* **2014**, *9*, 111450.

[6] F. Bashir, S. Kovács, Á. Ábrahám, K. Nagy, F. Ayaydin, I. Valkony-Kelemen, G. Ferenc, P. Galajda, S. Z. Tóth, L. Sass, P. B. Kós, I. Vass, M. Szabó, *Lab Chip* **2022**, *22*, 2986.

[7] E. W. H. Jager, O. Inganäs, I. Lundström, *Science* **2000**, *288*, 2335.

[8] a) Q. Jin, Y. Yang, J. A. Jackson, C. Yoon, D. H. Gracias, *Nano Lett.* **2020**, *20*, 5383; b) K. Malachowski, M. Jamal, Q. Jin, B. Polat, C. J. Morris, D. H. Gracias, *Nano Lett.* **2014**, *14*, 4164; c) H. Xu, S. Wu, Y. Liu, X. Wang, A. K. Efremov, L. Wang, J. S. McCaskill, M. Medina-Sánchez, O. G. Schmidt, *Nat. Nanotechnol.* **2024**, *19*, 494.

[9] L. Kelbauskas, R. Shetty, B. Cao, K.-C. Wang, D. Smith, H. Wang, S.-H. Chao, S. Gangaraju, B. Ashcroft, M. Kritzer, H. Glenn, R. H. Johnson, D. R. Meldrum, *Sci. Adv.* **2017**, *3*, 1602580.

[10] a) H. Ding, Z. Chen, P. S. Kollipara, Y. Liu, Y. Kim, S. Huang, Y. Zheng, *ACS Nano* **2022**, *16*, 10878; b) J. Chen, J. Zhou, Y. Peng, X. Dai, Y. Tan, Y. Zhong, T. Li, Y. Zou, R. Hu, X. Cui, H.-P. Ho, B. Z. Gao, H. Zhang, Y. Chen, M. Wang, X. Zhang, J. Qu, Y. Shao, *Adv. Mater.* **2024**, *36*, 2309143.

[11] a) J. Guck, S. Schinkinger, B. Lincoln, F. Wottawah, S. Ebert, M. Romeyke, D. Lenz, H. M. Erickson, R. Ananthakrishnan, D. Mitchell, J. Käs, S. Ulvick, C. Bilby, *Biophys. J.* **2005**, *88*, 3689; b) P. Jing, Y. Liu, E. G. Keeler, N. M. Cruz, B. S. Freedman, L. Y. Lin, *Biomed. Opt. Express* **2018**, *9*, 771; c) D. Wolfson, M. Steck, M. Persson, G. McNerney, A. Popovich, M. Goksor, T. Huser, *J. Biophotonics.* **2015**, *8*, 208.

[12] a) U. G. Būtaitė, G. M. Gibson, Y.-L. D. Ho, M. Taverne, J. M. Taylor, D. B. Phillips, *Nat. Commun.* **2019**, *10*, 1215; b) S. Hu, H. Xie, T. Wei, S. Chen, D. Sun, *Appl. Sci.* **2019**, *9*, 2883; c) G. Vizsnyiczai, A. Búzás, B. Lakshmanrao Aekbote, T. Fekete, I. Grexa, P. Ormos, L. Kelemen, *Biomed. Opt. Express* **2020**, *11*, 945.

[13] a) M. Dao, C. T. Lim, S. Suresh, *J. Mech. Phys. Solids* **2003**, *51*, 2259; b) A. Thakur, S. Chowdhury, P. Švec, C. Wang, W. Losert, S. K. Gupta, *Int. J. Robot. Res.* **2014**, *33*, 1098.

[14] I. Shishkin, H. Markovich, Y. Roichman, P. Ginzburg, *Micromachines* **2020**, *11*, 90.

[15] A. Di Cerbo, V. Rubino, F. Morelli, G. Ruggiero, R. Landi, G. Guidetti, S. Canello, G. Terrazzano, A. Alessandrini, *Stem Cells Int.* **2018**, *8*, 1219.

[16] B. L. Aekbote, T. Fekete, J. Jacak, G. Vizsnyiczai, P. Ormos, L. Kelemen, *Biomed. Opt. Express* **2016**, *7*, 45.

[17] a) J. K. Hohmann, M. Renner, E. H. Waller, G. von Freymann, *Adv. Opt. Mater.* **2015**, *3*, 1488; b) Y. Lin, J. Xu, *Adv. Opt. Mater.* **2018**, *6*, 1701359.

[18] a) R. Bernasconi, S. Pané, L. Magagnin, in *Advances in Chemical Engineering* (Eds.: L. Magagnin, F. Rossi), Academic Press, Cambridge, MA **2021**, p. *57*. b) W. Pang, S. Xu, J. Wu, R. Bo, T. Jin, Y. Xiao, Z. Liu, F. Zhang, X. Cheng, K. Bai, H. Song, Z. Xue, L. Wen, Y. Zhang, *Proc. Natl. Acad. Sci. USA* **2022**, *119*, 2215028119; c) F. Rajabasadi, L. Schwarz, M. Medina-Sánchez, O. G. Schmidt, *Prog. Mater. Sci.* **2021**, *120*, 100808.

[19] M. Tyagi, G. M. Spinks, E. W. H. Jager, *Soft Rob.* **2020**, *8*, 19.

[20] a) IP resins Young's moduli, https://www.nanoscribe.com/en/products/ip-photoresins (accessed: January 2024); b) J. Gao, L. Guan, J. Chu, Sixth International Symposium on Precision Engineering Measurements and Instrumentation, August 01, 2010, Hangzhou, China, **2010**; c) E. D. Lemma, F. Rizzi, T. Dattoma, B. Spagnolo, L. Sileo, A. Qualtieri, M. D. Vittorio, F. Pisanello, *IEEE Trans. Nanotechnol.* **2017**, *16*, 23.

[21] S. Nakanishi, S. Shoji, S. Kawata, H.-B. Sun, *Appl. Phys. Lett.* **2007**, *91*, 063112.

[22] H.-B. Sun, K. Takada, S. Kawata, *Appl. Phys. Lett.* **2001**, *79*, 3173.

[23] I. S. Ladner, M. A. Cullinan, S. K. Saha, *RSC Adv.* **2019**, *9*, 28808.

[24] J. Kubacková, C. Slabý, D. Horvath, A. Hovan, G. T. Iványi, G. Vizsnyiczai, L. Kelemen, G. Žoldák, Z. Tomori, G. Bánó, *Nanomaterials* **2021**, *11*, 2961.

[25] B. Buchroithner, D. Hartmann, S. Mayr, Y. J. Oh, D. Sivun, A. Karner, B. Buchegger, T. Griesser, P. Hinterdorfer, T. A. Klar, J. Jacak, *Nanoscale Adv.* **2020**, *2*, 2422.

[26] Y. J. Liu, J. Y. Yang, Y. M. Nie, C. H. Lu, E. D. Huang, C. S. Shin, P. Baldeck, C. L. Lin, *Microfluid. Nanofluid.* **2015**, *18*, 427.

[27] F. Klein, B. Richter, T. Striebel, C. M. Franz, G. von Freymann, M. Wegener, M. Bastmeyer, *Adv. Mater.* **2011**, *23*, 1341.

[28] S. J. Baldock, A. C. S. Talari, R. Smith, K. L. Wright, L. Ashton, *J. Raman Spectrosc.* **2019**, *50*, 371.

[29] S. Ushiba, K. Masui, N. Taguchi, T. Hamano, S. Kawata, S. Shoji, *Stem Cells Int.* **2015**, *5*, 17152.

[30] C. W. Ha, D.-Y. Yang, *Opt. Express* **2014**, *22*, 20789.

[31] J. Howard, *Motor Proteins and the Cytoskeleton*, Sinauer Associates, Inc., Sunderland, MA **2001**.

[32] Poisson's ratio polymers, https://www.sonelastic.com/en/fundamentals/tables-of-materials-properties/polymers.html (accessed: January 2024).

[33] Beam Torsion, https://engineeringlibrary.org/reference/beam-torsion-air-force-stress-manual (accessed: January 2024).

[34] M. B. Rasmussen, L. B. Oddershede, H. Siegumfeldt, *Appl. Environ. Microb.* **2008**, *74*, 2441.

[35] T. Fekete, M. Mészáros, Z. Szegletes, G. Vizsnyiczai, L. Zimányi, M. A. Deli, S. Veszelka, L. Kelemen, *ACS Appl. Mater. Interfaces* **2021**, *13*, 39018.

[36] K. C. Neuman, S. M. Block, *Rev. Sci. Instrum.* **2004**, *75*, 2787.

[37] K. Wang, Y. Xue, Y. Peng, X. Pang, Y. Zhang, L. I. Ruiz-Ortega, Y. Tian, A. H. W. Ngan, B. Tang, *Biochem. Bioph. Res. Co.* **2019**, *516*, 177.

[38] M. Islam, R. Mezencev, B. McFarland, H. Brink, B. Campbell, B. Tasadduq, E. K. Waller, W. Lam, A. Alexeev, T. Sulchek, *Cell Death Dis.* **2018**, *9*, 239.